Experimental explanation of the formation mechanism of surface mound-structures by femtosecond laser on polycrystalline $Ni_{60}Nb_{40}$

Edwin Peng, Alfred Tsubaki, Craig A. Zuhlke, Meiyu Wang, Ryan Bell, Michael J. Lucis, Troy P. Anderson, Dennis R. Alexander, George Gogos, and Jeffrey E. Shield

Experimental explanation of the formation mechanism of surface mound-structures by femtosecond laser on polycrystalline $Ni_{60}Nb_{40}$

Edwin Peng,[1] Alfred Tsubaki,[2] Craig A. Zuhlke,[2] Meiyu Wang,[1] Ryan Bell,[2] Michael J. Lucis,[1] Troy P. Anderson,[2] Dennis R. Alexander,[2] George Gogos,[1] and Jeffrey E. Shield[1]

[1]Department of Mechanical and Materials Engineering, University of Nebraska-Lincoln, Lincoln, Nebraska 68588, USA
[2]Department of Electrical and Computer Engineering, University of Nebraska-Lincoln, Lincoln, Nebraska 68588, USA

Femtosecond laser surface processing (FLSP) is an emerging technique for creating functionalized surfaces with specialized properties, such as broadband optical absorption or superhydrophobicity/superhydrophilicity. It has been demonstrated in the past that FLSP can be used to form two distinct classes of mound-like, self-organized micro/nanostructures on the surfaces of various metals. Here, the formation mechanisms of below surface growth (BSG) and above surface growth (ASG) mounds on polycrystalline $Ni_{60}Nb_{40}$ are studied. Cross-sectional imaging of these mounds by focused ion beam milling and subsequent scanning electron microscopy revealed evidence of the unique formation processes for each class of microstructure. BSG-mound formation during FLSP did not alter the microstructure of the base material, indicating preferential valley ablation as the primary formation mechanism. For ASG-mounds, the microstructure at the peaks of the mounds was clearly different from the base material. Transmission electron microscopy revealed that hydrodynamic melting of the surface occurred during FLSP under ASG-mound forming conditions. Thus, there is a clear difference in the formation mechanisms of ASG- and BSG-mounds during FLSP. © 2016 AIP Publishing LLC. [http://dx.doi.org/10.1063/1.4939983]

Femtosecond laser surface processing (FLSP) is a rapidly developing technique for the creation of functionalized surfaces through the fabrication of periodic, self-organized multi-scale structures.[1–4] A wide range of materials are applicable for FLSP: metals such as steel and nickel,[5–7] semiconductors, including silicon and germanium,[8–10] and polymers.[11–13] The resulting micro/nanostructure imbues surfaces with customizable surface properties such as increased broadband light absorption,[9,14] and tailored wetting properties ranging from superhydrophobic[15–17] to superhydrophilic.[18–20] These specialized properties have a plethora of potential applications, including for photovoltaics,[14,21] drag reduction,[22–24] heat transfer,[25–27] and biomedical implants.[28,29]

FLSP micro/nanostructures vary widely in morphology and size depending on target material and processing conditions. The most widely studied self-organized surface structures are nano/micro-scale ripples known as laser-induced periodic surface structures (LIPSS).[2,30–32] Depending on the target material and laser parameters, LIPSS can be oriented either perpendicular or parallel to the polarization of the incident pulses. The most commonly reported LIPSS have periods of the same order of magnitude as the laser wavelength. LIPSS on metal surfaces such as stainless steel and nickel form at low laser fluence, i.e., near the ablation threshold, and relatively low number of laser pulse counts (∼10 to 1000).

After a larger number of pulses (∼1000+), nanoparticle-covered pyramidal structures (NC-pyramids) can form in the same laser fluence range as LIPSS.[30,33,34] These NC-pyramids have a height-to-width aspect ratio of about 1:1. They can grow taller than $50\,\mu m$ and are covered with a layer of nanoparticles typically more than $2\,\mu m$ thick. NC-pyramids form when additional laser pulses on LIPSS create small precursor cones that are believed to originate from localized increases in ablation threshold.[30,33,34] These precursor cones increase steadily in height as the valleys deepen through preferential valley ablation (PVA). During the ablation process, nanoparticles are generated and redeposited on the surface, increasing the height of these cones. Due to this build-up of nanoparticles, a fully developed NC-pyramid can exceed the height of the original surface.

At laser fluence values above the ablation threshold and beyond the level for LIPSS, two types of self-organized, mound-like structures can form.[6,34,35] A commonly studied type of mound can be called below-surface growth (BSG) mounds, which are more tightly packed and have peaks that are beneath the original target surface. A second class of mounds which form at higher laser fluence than BSG-mounds can be called above-surface growth (ASG) mounds. ASG-mounds are separated by pits and feature peaks which can grow above the original surface. Previous studies by Zuhlke *et al.* of FLSP on Ni alloys, utilizing shot-by-shot scanning electron microscopy (SEM) imaging, indicated that BSG- and ASG-mounds have drastically different formation mechanisms.[6,33] ASG-mounds are formed using higher laser fluence (∼2 to $3\,J\,cm^{-2}$) and lower total laser pulses (∼30 to 150) than BSG-mounds (∼1 to $2\,J\,cm^{-2}$ and 120 to 600). The first phase of formation was found to be similar for both BSG- and ASG-mounds, where LIPSS, pits, and domes form on the surface. For BSG mounds, it is thought that PVA is the dominant formation process.[6,16,36,37] For ASG-mounds, the higher fluence generates more extreme thermal

excursions and so growth instead is thought to be dominated by resolidification of the target material through fluid flow and vapor-liquid-solid (VLS) growth.[6,35] As total laser pulses increase, BSG and ASG mounds devolve into pits.

Further understanding of the growth mechanisms of BSG- and ASG-mounds is necessary for the fundamental understanding of laser-material interactions and optimization of surface functionalization. The similarities in overall surface morphologies make it difficult to unequivocally understand their formation mechanisms. However, the thermal history of mounds can be determined by cross-sectional imaging and comparing the microstructures observed in the mounds with that of the base (initial) material. Furthermore, by selecting appropriate materials that undergo dramatic microstructural changes upon the imposition of thermal events, one can more readily observe any thermally induced changes.

In this study, $Ni_{60}Nb_{40}$, an alloy with easy glass-forming ability, was chosen as the base material.[38–41] $Ni_{60}Nb_{40}$ ingots were made by arc-melting pure Ni (99.995+%) and Nb (99.95+%) in Zr-gettered Ar atmosphere. Ribbons of amorphous $Ni_{60}Nb_{40}$, up to 150 μm thick and 4 mm wide, were fabricated from the ingots by melt-spinning in Ar atmosphere at a tangential wheel speed of 10 m s^{-1}. For heat treatment at 1373 K for 20 h in tube furnace, ribbons were sealed in quartz tube under Ar atmosphere after repeated evacuation cycles to prevent oxidation. Polycrystalline $Ni_{60}Nb_{40}$ microstructure was characterized using SEM and energy dispersive X-ray spectroscopy (EDS) in the FEI Helios NanoLab 660 DualBeam with EDAX Octane EDS Detector. Phase analysis was accomplished by X-ray diffraction (XRD) using Cu Kα radiation in Bruker-AXS D8 Discover X-ray diffractometer, with all samples mounted on a zero-background holder made of an off-cut Si single crystal. To prepare the surfaces for FLSP, ribbons were polished through standard metallurgical procedures, with final polish using 0.3 μm α-Al_2O_3 powder. After polishing, the ribbons were cleaned in an ultrasonic bath by successively submerging in acetone, methanol, and deionized water for 20 min each.

A Ti:Sapphire femtosecond laser system, Spectra Physics Spitfire, capable of producing 1 mJ, 80 fs laser pulses, was used to fabricate the BSG- and ASG-mounds. The laser repetition rate was adjustable from single pulses to maximum of 1 kHz with a computer-controlled shutter. A Frequency Resolved Optical Grating (FROG) instrument, Positive Light Model 8–02, was used to monitor laser pulse length and chirp. The laser power was controlled using a half waveplate and polarizer. Positioning and translation relative to the laser focal volume of laser-processed samples were controlled using computer-guided Nanomotion II translation stages from Melles Griot with 3 axes of motion. A parabolic mirror, Thorlabs MPD169-P01, with 152.4 mm focal length was used to focus the femtosecond pulses with a Gaussian profile. By changing stage speed, spot size, and pulse energy, the fluence and number of ablation pulses per unit area incident on the sample were tuned to create each class of microstructures. The laser spot size, which was used to calculate the laser fluence and pulse count, was determined using the method outlined by Liu.[42]

The laser processing parameters used to produce BSG-mounds were 625 laser pulses at peak fluence of 2.14 J cm^{-2}, with translation speed and pitch of 3 mm s^{-1} and 15 μm, respectively. This laser fluence was chosen as it was close to the minimum required for BSG-mound formation on polycrystalline $Ni_{60}Nb_{40}$. The ASG-mounds were fabricated using 175 laser pulses at a peak laser fluence of 6.10 J cm^{-2}, with translation speed and pitch of 4.5 mm s^{-1} and 15 μm, respectively. The chosen laser fluence was at the high end for ASG-mound formation to ensure the surface structure was distinct from BSG-mounds. The laser pulse counts were chosen for maximum growth of both types of mounds. Evolution of FLSP structures as a function of laser pulse counts was similar to what was previously used for FLSP of Ni 200/201, on which the final, saturated BSG and ASG structures were reached after 600 and 150 pulses, respectively.[6]

The FEI Helios NanoLab 660 DualBeam provided SEM imaging, cross section milling of the BSG- and ASG-mounds, and transmission electron microscopy (TEM) samples. An ASG-mound was protected by deposition of 100 nm thick Pt layer by electron beam-induced deposition, followed by 2 μm thick Pt layer via ion beam-induced deposition. The target mound was steadily removed by FIB milling, leaving a 1 μm thick cross section at the center. The cross section was removed from the surface using a W needle and welded onto a Cu Omniprobe Lift-Out grid using ion beam-induced Pt deposition. Finally, the TEM sample was thinned using FIB milling until reaching electron transparency of <100 nm thick. TEM imaging was performed with an FEI Tecnai Osiris S/TEM operating at 200 kV.

The melt-spun $Ni_{60}Nb_{40}$ ribbons were found to be amorphous, as shown in Figure 1(a). Heat treatment at 1373 K for 20 h resulted in a two-phase structure of orthorhombic Ni_3Nb and rhombohedral Ni_6Nb_7 (Figure 1(b)), consistent with what was expected from the equilibrium phase diagram.[41,43,44] An ion-induced secondary electron (ISE) image revealed a two-phase structure (Figure 2), consistent with the XRD results. The average Ni_3Nb grain size was around 2 μm. The grain structure within the Ni_6Nb_7 regions was not evident due to weak channeling contrast. Location specific EDS spectra were collected, and a semi-quantitative EDS analysis was performed with the TEAM EDS software. The analysis revealed that the light-colored grains have average atomic concentration of 75.9 ± 0.9 at. % Ni and 24.1 ± 0.5

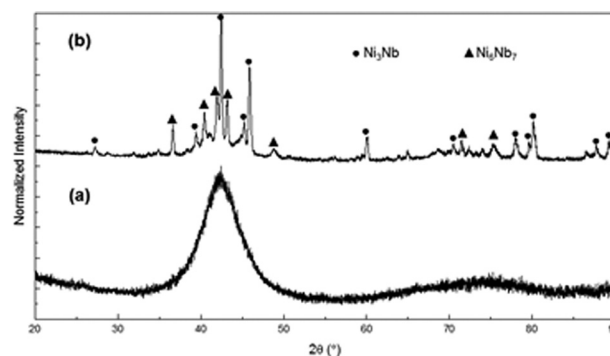FIG. 1. XRD patterns of (a) as-solidified ribbons displaying an amorphous structure and (b) polycrystalline $Ni_{60}Nb_{40}$ after heat treatment showing crystalline peaks corresponding to Ni_3Nb (●) and Ni_6Nb_7 (▲).
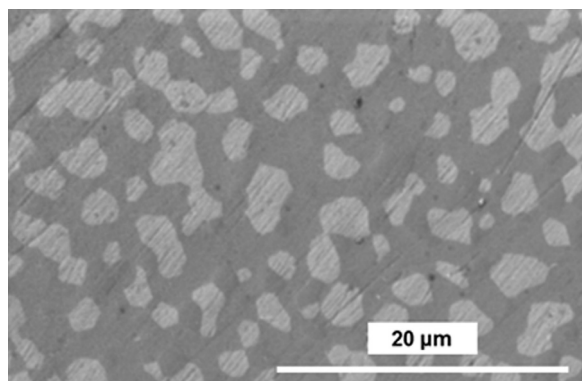
FIG. 2. SEM top surface image of polycrystalline $Ni_{60}Nb_{40}$ displaying Ni_6Nb_7 (grey) and Ni_3Nb (white) phases.

at. % Nb, close to the expected composition of the Ni_3Nb phase. The Ni_3Nb grains were embedded in darker region having atomic concentration of 45.7 ± 1.0 at. % Ni and 54.3 ± 1.5 at. % Nb, which correspond to the Ni_6Nb_7 phase.

Figure 3 contains SEM images of the BSG- and ASG-mounds created by FLSP. ASG-mounds show larger peak-to-peak distances, and separated by deep pits, consistent with previous results of FLSP on Ni.[6] Both BSG- and ASG-mounds feature ridges that were perpendicular to the laser's polarization. The thermal histories of surfaces modified by FLSP can be determined by examining the cross-sectional microstructure of these BSG- and ASG-mounds. Dual-beam instruments are ideal for cross-sectioning targeted regions, in this case the BSG- and ASG-mounds. For cross sectioning, the BSG- or ASG-mound was first protected by deposition of 100 nm thick Pt layer by electron beam-induced deposition, followed by 3 μm thick Pt layer via ion beam-induced deposition. Then, FIB milling was used to remove approximately half of the target mound. The resulting cross-sectioned mounds were examined at a tilt of 52° using ISE imaging.

The cross sectional images of representative BSG- and ASG-mounds are shown in Figures 4(a) and 4(b), respectively. At the top of each mound, the distinct darker layers are the Pt that was deposited to protect these mounds from ion

beam damage during the FIB milling process. The microstructures of the BSG-mound were identical to that of the base material shown in Figure 2: a two-phase polycrystalline $Ni_{60}Nb_{40}$ microstructure. EDS showed that the lighter grains were Ni_3Nb and the darker region was Ni_6Nb_7, again consistent with what was observed for the base material prior to FLSP. Furthermore, there was no significant change in morphology nor average size of the Ni_3Nb grains. It should be noted that the vertical streaks observed in Figure 4 are due to blanketing that occurred during FIB milling. Overall, the microstructural stability suggests that any thermal excursions during FLSP which produced the BSG-mounds were minimal, and definitely below temperatures that would induce grain growth or melting. Furthermore, the lack of significant heating is consistent with BSG-mound formation via the PVA mechanism.[6,34,35,37] PVA occurs due to higher laser fluence at the valleys than the peaks of precursor mounds. This difference in fluence is a combination of different incident area and reflection of incident photons toward the valleys. These BSG-mounds appear to grow in the same way, by the valleys of precursor mounds preferentially ablated due to higher fluence, as other laser-processed, mound-like structures produced on Si,[21,37,45] Ti,[46] and most similarly, Ni.[6]

In contrast, the microstructure of the ASG-mound shows that the top portion ($\sim$10 μm thick) was distinct from the $Ni_{60}Nb_{40}$ microstructure and the Pt protective layers. The lower portion of the ASG-mound consisted of the same microstructure as the base material prior to FLSP. EDS analysis revealed that the top region was comprised of 56.5 ± 2.5 at. % Ni and 43.5 ± 1.4 at. % Nb, similar to the original nominal ingot composition of 60 at. % Ni and 40 at. % Nb. The same two-portion microstructure was consistently observed in other cross-sectioned ASG-mounds. Figure 5(a) shows a TEM bright field image of the top portion of the liftout sample. There were no evident crystalline grains, in contrast to the image of the bulk $Ni_{60}Nb_{40}$ microstructure shown in Figure 5(b). Selected Area Electron Diffraction (SAED) pattern, Figure 5(c), taken at the top portion confirmed its amorphous structure.

The amorphous nature of the top portion is due to the readiness with which the $Ni_{60}Nb_{40}$ alloy forms glass, as the
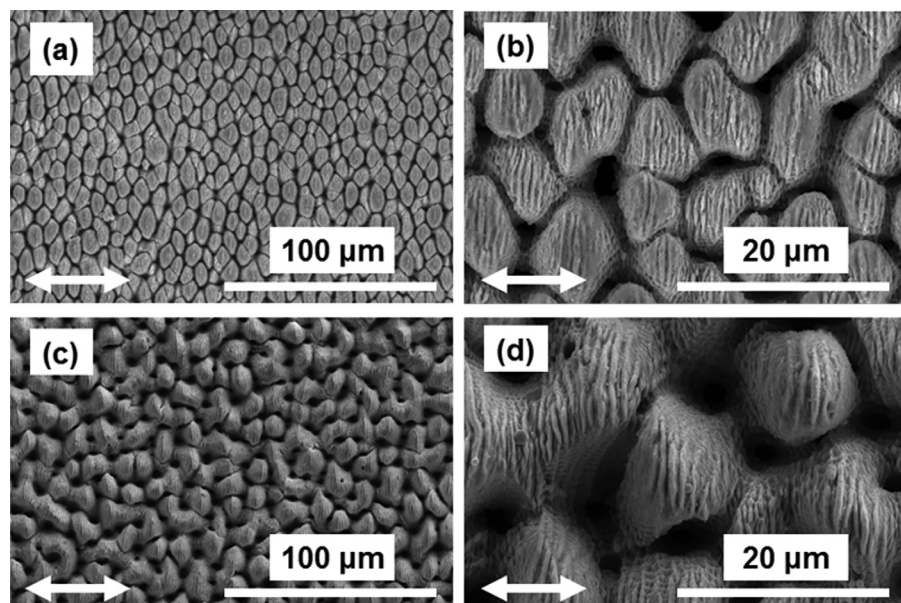

FIG. 3. SEM top surface images of BSG-mounds (a) and (b) and ASG-mounds (c) and (d). The double-ended arrow indicates laser polarization direction.
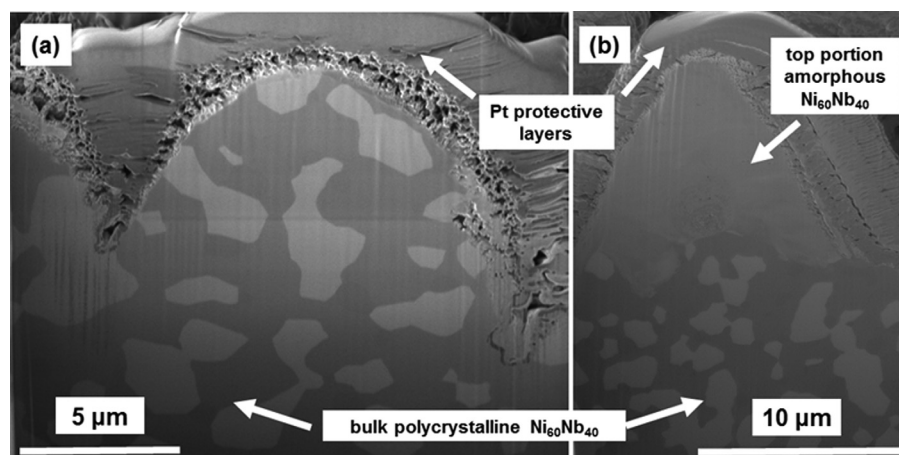
FIG. 4. SEM images of typical (a) BSG-mound cross section and (b) ASG-mound cross section.
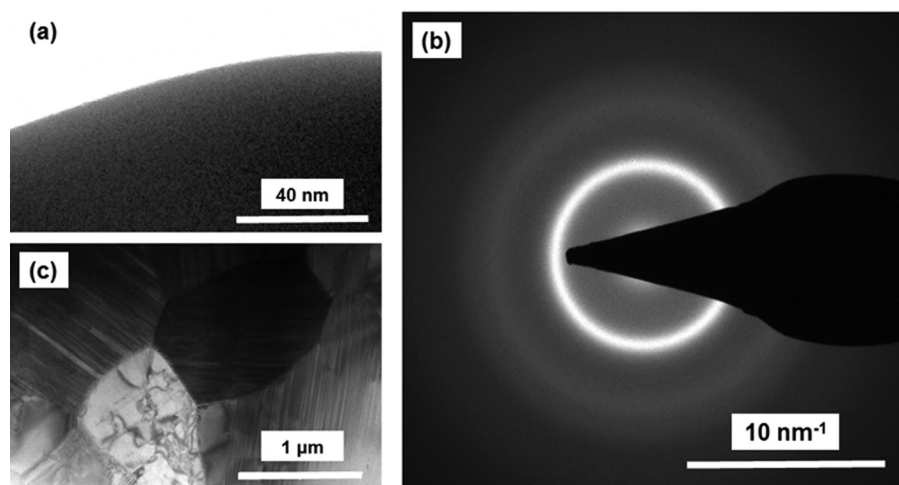

FIG. 5. (a) TEM bright field image and (b) SAED pattern of the amorphous $Ni_{60}Nb_{40}$ top portion of the ASG-mound. TEM bright field image of the (c) bulk polycrystalline $Ni_{60}Nb_{40}$ microstructure of the lower portion of the ASG-mound.

as-solidified melt spun ribbons were amorphous at a relatively low wheel speed. Furthermore, the base material provides a heat sink, and combined with the small volume of melted material it was expected the cooling rate was relatively high. At slower solidification rates, a polycrystalline, eutectic structure would be evident.[44] We believe this top, amorphous portion was responsible for the greater heights of ASG-mounds and was most likely the result of fluid flow, the hydrodynamical process in which the target surface melts, and the resulting liquid is driven from the valleys to the peaks of the ASG-mounds. Such fluid flow has been previously been reported to explain similar high aspect ratio structures, called "columns" or "spikes," generated by nanosecond and femtosecond lasers on Si substrates and Ni200/201.[6,21,47,48] Two mechanisms were proposed to explain fluid flow depositing this amorphous portion on top of ASG-mounds. First, similar to PVA, higher laser fluence at the bottom of the valleys can cause a temperature gradient with the side and top of the peaks. Such a gradient can direct the molten layer to flow toward the top of mounds, as was previously reported by Sánchez *et al.* for laser processing of Si.[47,48] Second, the liquid may be forced upwards from the valley to the peaks by laser-induced shock waves.[49,50] Besides fluid flow, VLS growth, where laser-processed structures receive deposition of target material from a vapor cloud produced during the ablation process, could have contributed to forming this top amorphous portion.[6,33,34,51]

Utilizing FIB milling to observe the microstructure within the mounds, we provided direct evidence of the formation process of BSG- and ASG-mounds created on polycrystalline $Ni_{60}Nb_{40}$ during FLSP. Cross sectional imaging of ASG-mounds revealed an amorphous portion at the top of the mound and the bulk polycrystalline $Ni_{60}Nb_{40}$ microstructure at the bottom. We attribute this amorphous portion to melting and subsequent fluid flow during FLSP, and thus the primary formation mechanism of ASG-mounds is due to redistribution of material from the valleys to the peaks. In the BSG-mounds, no change occurred in the microstructure compared to the base material's microstructure prior to FLSP was observed. It is homogenous throughout the mound, suggesting inconsequential heating during FLSP. This observation for BSG-mounds is consistent with PVA as the formation mechanism. Thus, analysis of the microstructures within the BSG- and ASG-mounds supports the different proposed formation mechanisms for each of the laser processing conditions.

[1]K. Sugioka and Y. Cheng, Light: Sci. Appl. **3**, e149 (2014).

[2]A. Y. Vorobyev and C. Guo, Laser Photonics Rev. **7**(3), 385–407 (2013).

[3]K. Sugioka and Y. Cheng, *Femtosecond Laser 3D Micromachining for Microfluidic and Optofluidic Applications* (Springer, London, 2014), pp. 19–33.

[4]A. Y. Vorobyev and C. Guo, Sci. Adv. Mater. **4**(3–4), 432–438 (2012).

[5]B. Wu, M. Zhou, J. Li, X. Ye, G. Li, and L. Cai, Appl. Surf. Sci. **256**(1), 61–66 (2009).

[6]C. A. Zuhlke, T. P. Anderson, and D. R. Alexander, Opt. Express **21**(7), 8460–8473 (2013).

[7]K. Kuršelis, R. Kiyan, and B. N. Chichkov, Appl. Surf. Sci. **258**(22), 8845–8852 (2012).

[8]H. Wang, P. Kongsuwan, G. Satoh, and Y. L. Yao, Int. J. Adv. Manuf. Technol. **65**(9–12), 1691–1703 (2013).

[9]H. Wang, P. Kongsuwan, G. Satoh, and Y. L. Yao, J. Manuf. Sci. Eng. **134**(3), 031006 (2012).

[10]K. N. Barada, C. G. Mool, and W. K. Kurt, Nanotechnology **18**(19), 195302 (2007).

[11]E. Rebollar, J. Mildner, N. Götte, D. Otto, C. Sarpe, J. Köhler, M. Wollenhaupt, T. Baumert, and M. Castillejo, Appl. Surf. Sci. **302**, 231–235 (2014).

[12]E. Rebollar, M. Castillejo, and T. A. Ezquerra, Eur. Polym. J. **73**, 162–174 (2015).

[13]E. Rebollar, J. R. Vazquez de Aldana, I. Martin-Fabiani, M. Hernandez, D. R. Rueda, T. A. Ezquerra, C. Domingo, P. Moreno, and M. Castillejo, Phys. Chem. Chem. Phys. **15**(27), 11287–11298 (2013).

[14]V. V. Iyengar, B. K. Nayak, and M. C. Gupta, Sol. Energy Mater. Sol. Cells **94**(12), 2251–2257 (2010).

[15]P. Bizi-Bandoki, S. Benayoun, S. Valette, B. Beaugiraud, and E. Audouard, Appl. Surf. Sci. **257**(12), 5213–5218 (2011).

[16]A.-M. Kietzig, S. G. Hatzikiriakos, and P. Englezos, Langmuir **25**(8), 4821–4827 (2009).

[17]J. Yong, F. Chen, Q. Yang, Y. Fang, J. Huo, and X. Hou, Chem. Commun. **51**, 9813–9816 (2015).

[18]A. Y. Vorobyev and C. Guo, in *Advanced Lasers*, edited by O. Shulika and I. Sukhoivanov (Springer, Netherlands, 2015), Vol. 193, pp. 101–115.

[19]G. Li, Y. Lu, P. Wu, Z. Zhang, J. Li, W. Zhu, Y. Hu, D. Wu, and J. Chu, J. Mater. Chem. A **3**, 18675–18683 (2015).

[20]Y. Tian and L. Jiang, MRS Bull. **40**(02), 155–165 (2015).

[21]M.-J. Sher, M. T. Winkler, and E. Mazur, MRS Bull. **36**(06), 439–445 (2011).

[22]R. Truesdell, A. Mammoli, P. Vorobieff, F. van Swol, and C. J. Brinker, Phys. Rev. Lett. **97**(4), 044504 (2006).

[23]R. J. Daniello, N. E. Waterhouse, and J. P. Rothstein, Phys. Fluids **21**(8), 085103 (2009).

[24]A. Rastegari and R. Akhavan, J. Fluid Mech. **773**(R4), 1–14 (2015).

[25]C. Kruse, T. Anderson, C. Wilson, C. Zuhlke, D. Alexander, G. Gogos, and S. Ndao, Langmuir **29**(31), 9798–9806 (2013).

[26]R. Enright, N. Miljkovic, J. L. Alvarado, K. Kim, and J. W. Rose, Nanoscale Microscale Thermophys. Eng. **18**(3), 223–250 (2014).

[27]C. M. Kruse, T. Anderson, C. Wilson, C. Zuhlke, D. Alexander, G. Gogos, and S. Ndao, Int. J. Heat Mass Transfer **82**, 109–116 (2015).

[28]V. Dumas, A. Rattner, L. Vico, E. Audouard, J. C. Dumas, P. Naisson, and P. Bertrand, J. Biomed. Mater. Res., Part A **100**(11), 3108–3116 (2012).

[29]A. Y. Vorobyev and C. Guo, Appl. Surf. Sci. **253**(17), 7272–7280 (2007).

[30]C. A. Zuhlke, T. P. Anderson, and D. R. Alexander, Appl. Surf. Sci. **283**, 648–653 (2013).

[31]J. F. Young, J. S. Preston, H. M. van Driel, and J. E. Sipe, Phys. Rev. B **27**(2), 1155–1172 (1983).

[32]G. D. Tsibidis, M. Barberoglou, P. A. Loukakos, E. Stratakis, and C. Fotakis, Phys. Rev. B **86**, 115316 (2012).

[33]C. A. Zuhlke, T. P. Anderson, and D. R. Alexander, Appl. Phys. Lett. **103**(12), 121603 (2013).

[34]E. J. Y. Ling, J. Saïd, N. Brodusch, R. Gauvin, P. Servio, and A.-M. Kietzig, Appl. Surf. Sci. **353**, 512–521 (2015).

[35]Y. Li, Z. Cui, W. Wang, C. Lin, and H.-L. Tsai, Appl. Surf. Sci. **324**, 775–783 (2015).

[36]B. K. Nayak and M. C. Gupta, Opt. Lasers Eng. **48**(10), 940–949 (2010).

[37]B. R. Tull, J. E. Carey, E. Mazur, J. P. McDonald, and S. M. Yalisove, MRS Bull. **31**(08), 626–633 (2006).

[38]M. Enayati, Sci. Iran. **9**(2), 157–161 (2002).

[39]T. Nagase, T. Sanda, A. Nino, W. Qin, H. Yasuda, H. Mori, Y. Umakoshi, and J. A. Szpunar, J. Non-Cryst. Solids **358**(3), 502–518 (2012).

[40]C. C. Koch, O. B. Cavin, C. G. McKamey, and J. O. Scarbrough, Appl. Phys. Lett. **43**(11), 1017–1019 (1983).

[41]M. H. Lee, W. T. Kim, D. H. Kim, and Y. B. Kim, Mater. Sci. Eng., A **375–377**, 336–340 (2004).

[42]J. M. Liu, Opt. Lett. **7**(5), 196–198 (1982).

[43]Z. Kejun and J. Zhanpeng, Scr. Metall. Mater. **26**(3), 417–422 (1992).

[44]H. Okamoto, J. Phase Equilib. **19**(3), 289 (1998).

[45]J. Zhu, G. Yin, M. Zhao, D. Chen, and L. Zhao, Appl. Surf. Sci. **245**(1–4), 102–108 (2005).

[46]M. Tsukamoto, T. Kayahara, H. Nakano, M. Hashida, M. Katto, M. Fujita, M. Tanaka, and N. Abe, J. Phys.: Conf. Ser. **59**(1), 666–669 (2007).

[47]F. Sánchez, J. L. Morenza, R. Aguiar, J. C. Delgado, and M. Varela, Appl. Phys. A **66**(1), 83–86 (1998).

[48]F. Sánchez, J. L. Morenza, and V. Trtik, Appl. Phys. Lett. **75**(21), 3303–3305 (1999).

[49]Z. Wu, X. Zhu, and N. Zhang, J. Appl. Phys. **109**(5), 053113 (2011).

[50]T. Y. Choi and C. P. Grigoropoulos, J. Appl. Phys. **92**(9), 4918–4925 (2002).

[51]S. I. Dolgaev, S. V. Lavrishev, A. A. Lyalin, A. V. Simakin, V. V. Voronov, and G. A. Shafeev, Appl. Phys. A **73**(2), 177–181 (2001).